

Likelihood-based GNSS positioning using LOS/NLOS predictions from 3D mapping and pseudoranges

Paul D. Groves¹  · Mounir Adjrard¹

Received: 2 February 2017 / Accepted: 19 July 2017 / Published online: 27 July 2017
© The Author(s) 2017. This article is an open access publication

Abstract The accuracy of conventional global navigation satellite systems (GNSS) positioning in dense urban areas is severely degraded due to blockage and reflection of the signals by the surrounding buildings. By using 3D mapping of the buildings to aid GNSS positioning, the accuracy can be substantially improved. However, positioning performance must be balanced against computational load. Here, a likelihood-based 3D-mapping-aided (3DMA) GNSS ranging algorithm is demonstrated that enables signals predicted to be non-line-of-sight (NLOS) to contribute to the position solution without explicitly computing the additional path delay due to NLOS reception, which is computationally expensive. Likelihoods for an array of candidate positions are computed based on the difference between the measured and predicted pseudoranges. However, a skewed distribution is assumed for those signals predicted to be NLOS on the basis that the ensuing ranging errors are always positive. An overall position solution is then extracted from the likelihood surface. GNSS measurement data have been collected at several locations in both traditional and modern dense urban environments. Horizontal root-mean-square single-epoch position accuracies of 4.7, 5.6 and 6.5 m are obtained using, respectively, a Leica Viva geodetic receiver, a u-blox EVK M8T consumer-grade receiver and a Nexus 9 tablet incorporating a smartphone GNSS antenna and a GNSS chipset that outputs pseudoranges. The corresponding accuracies using single-epoch conventional GNSS positioning are 20.5, 23.0 and 28.4 m, about a factor of four larger. The 3DMA

GNSS algorithms have also been implemented in real time on a Raspberry Pi 3 at a 1-Hz update rate.

Keywords GNSS · 3D mapping · Urban positioning · NLOS reception · 3DMA GNSS

Introduction

Global navigation satellite systems (GNSS) positioning in dense urban areas is poor because buildings block, reflect and diffract the signals. By using 3D mapping, many of these effects may be predicted, enabling positioning accuracy to be substantially improved. A wide range of applications could benefit, including situation awareness of emergency, security and military personnel and vehicles; emergency caller location; navigation for the visually impaired; tracking vulnerable people and valuable assets; intelligent mobility; enforcement of court orders; lane-level road positioning for intelligent transportation systems; advanced rail signaling; mobile mapping; aerial surveillance; location-based services and augmented reality.

Buildings and other obstacles degrade GNSS positioning in three ways. Firstly, where signals are completely blocked, they are simply unavailable for positioning, degrading the signal geometry. Secondly, where the direct signal is blocked (or severely attenuated), but the signal is received via a stronger reflected path, non-line-of-sight (NLOS) reception occurs. NLOS signals exhibit positive ranging errors corresponding to the difference between the reflected and direct paths. These are typically a few tens of meters in dense urban areas, but can be much larger if a distant building reflects a signal. Thirdly, where both direct line-of-sight (LOS) and reflected signals are received, multipath interference occurs. This can lead to both

✉ Paul D. Groves
p.groves@ucl.ac.uk

¹ University College London, Gower Street,
London WC1E 6BT, UK

positive and negative ranging errors, the magnitude of which depends on the signal and receiver designs. The term “multipath” is often used to describe NLOS reception. However, this is misleading as the two phenomena have different characteristics and can require different mitigation approaches (Groves 2013a, b; Bhuiyan and Lohan 2012). 3D-mapping-aided (3DMA) GNSS techniques largely compensate for the effects of NLOS reception.

3D mapping can be used to aid GNSS positioning in several different ways. The simplest is terrain height aiding. For most land applications, the user antenna is at a known height above the terrain, so a digital terrain model (DTM) or digital elevation model (DEM) can be used to constrain the position solution to a surface. In conventional least squares positioning, this is done by generating a virtual ranging measurement (Amt and Raquet 2006). In open areas, this only improves the vertical position solution. However, in dense urban areas where the signal geometry is poor, terrain height aiding can improve the horizontal accuracy by almost a factor of two (Adjrad and Groves 2017).

3D building models can be used to predict which signals are blocked and which are directly visible at any location (Bradbury et al. 2007; Suh and Shibasaki 2007). This can be computationally intensive. However, the real-time computational load can be reduced dramatically by pre-computing building boundaries for each candidate position. These describe the minimum elevation above which satellite signals can be received at a series of azimuths. A signal can then be classified as LOS or NLOS simply by comparing the satellite elevation with that of the building boundary (Wang et al. 2012). The 3D building models can also be used to predict the additional path traveled by NLOS signals, enabling affected pseudoranges to be corrected. However, a practical precomputation technique for this has yet to be developed, so processing load remains a limitation.

GNSS shadow matching determines position by comparing the measured signal availability and strength with predictions made using a 3D city model over a range of candidate positions. This enables across-street position accuracies of a few meters to be achieved in dense urban areas (Groves 2011; Ben-Moshe et al. 2011; Suzuki and Kubo 2012; Wang et al. 2013, 2015; Yozevitch and Ben-Moshe 2015). However, the focus here is on 3D-mapping-aided GNSS ranging.

Where the user position is already approximately known, it is straightforward to use predictions from a 3D city model to eliminate NLOS measurements from a conventional least squares GNSS position solution (Obst et al. 2012; Bourdeau and Sahmoudi 2012; Peyraud et al. 2013). However, for most urban positioning applications there is significant position uncertainty. One solution is to define a

search area centered on the conventional GNSS position solution and compute the proportion of candidate positions at which each signal is receivable via direct LOS. This can then be used to re-weight a least squares position solution and aid signal selection and weighting by consistency checking (Adjrad and Groves 2017).

More sophisticated approaches score a set of position hypotheses using the GNSS pseudorange measurements and satellite visibility predictions at each candidate position. This enables different signals to be treated as NLOS at different candidate positions. Several groups have used 3D mapping to adjust the predictions of the pseudoranges at each candidate user position in order to account for the additional path delay due to NLOS reception (Suzuki and Kubo 2013; Gu et al. 2015; Hsu et al. 2015). A likelihood for each candidate position is then computed based on some measure of consistency between the measured pseudoranges and the predicted pseudoranges at that position, adjusted for NLOS reception. A single-epoch positioning accuracy of 4 m has been reported (Hsu et al. 2015). Kumar and Petovello (2014) have applied a version of this technique to multipath interference whereby the additional path delay measured using a correlator bank is compared with predictions across an array of candidate positions. However, as computation of the path delay due to NLOS reception is computationally intensive, real-time implementations of these techniques are limited to around a hundred candidate positions. The urban trench approach presented in Betaille et al. (2013) enables the path delays of NLOS signals to be computed very efficiently, but only if the building layout is highly symmetric, so it can only be used in suitable environments.

To handle large initial position uncertainties in real time, there is a need for a ranging-based positioning algorithm that scores a set of position hypothesis using only the LOS/NLOS predictions from a 3D city model, which can be computed quickly. Suzuki (2016) presents an algorithm that computes a least squares position solution using only the signals predicted by the 3D city model to be direct LOS at a given candidate position. Each candidate is then scored according to the Mahalanobis distance between the candidate position and the corresponding least squares solution.

Here, a new approach is presented that enables those signals predicted to be NLOS to also contribute to the score for each candidate position hypothesis, but without explicitly computing the additional path delay due to NLOS reception. This substantially reduces the processing load. As in previous approaches (Hsu et al. 2015), a likelihood for each candidate user position is computed based on the difference between the measured and predicted pseudoranges for both LOS and NLOS signals. However, the predicted pseudoranges are not adjusted to account for NLOS reception. Instead, a skewed measurement error

distribution is assumed for those signals predicted to be NLOS on the basis that the ensuing ranging errors are always positive. Positions are currently computed from a single epoch of GNSS measurement data.

A brief summary of the approach and some preliminary results have been included in a conference paper alongside other related work (Adjrad and Groves 2016). Here, the final version of the algorithm is described in full, together with the tuning process, and results are presented based on new experimental data collected using a Leica Viva geodetic receiver, a u-blox EVK M8T consumer-grade receiver and a Nexus 9 tablet incorporating a smartphone GNSS antenna and a GNSS chipset that outputs pseudoranges. The 3DMA GNSS algorithms have also been implemented in real time on a Raspberry Pi 3 at a 1-Hz update rate.

The paper is structured as follows. Full details of the algorithms are presented first. The experimental data collection is then described, followed by the tuning and optimization process. Selected sites and epochs are then examined in detail, followed by a summary of the overall positioning performance. Finally, the conclusions are presented and future and related work discussed.

Algorithm description

Figure 1 shows the components of the likelihood-based 3DMA GNSS ranging positioning algorithm. As position is determined by scoring a series of candidate positions, the first step is to determine those candidates. This requires an initial position estimate. Here, this is provided by UCL’s 3DMA least squares positioning algorithm (Adjrad and Groves 2017). This is about a factor of 2 more accurate than conventional GNSS positioning in dense urban

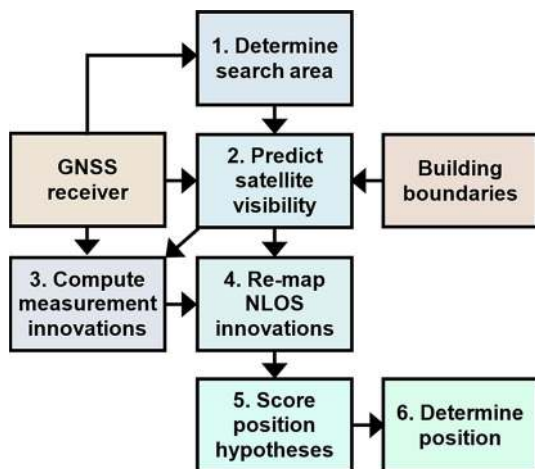


Fig. 1 Block diagram of likelihood-based 3DMA GNSS ranging positioning algorithm

environments, enabling a smaller search area to be used. In a continuous positioning system, the position solution from the previous epoch could be used.

A conventional single-epoch GNSS solution comprises 3 position components and the receiver clock offset. A search grid of more than two dimensions is impractical. Therefore, height is eliminated by associating a height with each horizontal position using a terrain height database and the receiver clock offset is eliminated by differencing pseudorange measurements across satellites. Here, a 40-m-radius circular search area with a 1-m spacing between candidate positions is used. This was sufficient to encompass the true position for all of the test data. As outdoor positioning is assumed, indoor candidates are eliminated, reducing the processing load. In future, the search area could be scaled according to the uncertainty of the position solution used for initialization (Groves et al. 2015).

The second step is to predict the satellite visibility at each candidate position. This is done efficiently by comparing the satellite elevation with that of a precomputed building boundary at the appropriate azimuth (Wang et al. 2012).

The third step is to compute measurement innovations. First, the range from each candidate position, p , to each satellite, j , is computed using

$$\hat{r}_{pj} = \sqrt{\left[\mathbf{C}_e^l(\hat{r}_{pj}) \hat{\mathbf{r}}_{ej}^e(\tilde{t}_{st,a}^j) - \mathbf{r}_{ep}^e(t_{sa,a}^j) \right]^T \left[\mathbf{C}_e^l(\hat{r}_{pj}) \hat{\mathbf{r}}_{ej}^e(\tilde{t}_{st,a}^j) - \mathbf{r}_{ep}^e(t_{sa,a}^j) \right]} \tag{1}$$

where $\mathbf{r}_{ep}^e = (x_{ep}^e \ y_{ep}^e \ z_{ep}^e)^T$ is the Cartesian ECEF position vector of candidate position p , $\hat{\mathbf{r}}_{ej}^e = (\hat{x}_{ej}^e \ \hat{y}_{ej}^e \ \hat{z}_{ej}^e)^T$ is the Cartesian ECEF position of satellite j , $t_{sa,a}^j$ is the time of signal arrival, $\tilde{t}_{st,a}^j$ is the measured time of signal transmission, which can be assumed the same for all candidate positions, a denotes the user antenna. The Sagnac effect is compensated using

$$\mathbf{C}_e^l(r_{pj}) \approx \begin{pmatrix} 1 & \omega_{ie} r_{pj} / c & 0 \\ -\omega_{ie} r_{pj} / c & 1 & 0 \\ 0 & 0 & 1 \end{pmatrix} \tag{2}$$

where $\omega_{i,e} = 7.292115 \times 10^{-5} \text{ rad s}^{-1}$ is the Earth rotation rate and $c = 299,792,458 \text{ m s}^{-1}$ is the speed of light. As (1) is recursive, \hat{r}_{pj} is first computed with $\mathbf{C}_e^l = \mathbf{I}$, and then, the calculation repeated using $\mathbf{C}_e^l(\hat{r}_{pj})$.

As measurements are differenced across satellites to eliminate the receiver clock offset, a reference satellite is required. In conventional positioning, the highest elevation satellite is used. Here, a separate reference satellite, $r(p)$, is designated for each candidate position and is the highest elevation satellite that is predicted to be LOS at that point and all immediately adjacent points.

Measurement innovations at each candidate position are then computed using

$$\delta z_{pj} = \tilde{\rho}_a^j - \tilde{\rho}_a^{r(p)} - \hat{r}_{pj} + \hat{r}_{pr(p)} \quad j \neq r(p) \tag{3}$$

where $\tilde{\rho}_a^j$ is the measured pseudorange from satellite j to the user antenna, a . The measured pseudoranges are corrected for satellite clock errors, ionosphere errors (using the Klobuchar model) and troposphere errors [using the Neil model (Neil 1996)]. SBAS ionosphere corrections could also be used. The GLONASS measurements are also corrected for the GLONASS-GPS interconstellation timing offset, which is obtained from the GLONASS navigation data message (Anon 2008). Interconstellation timing offsets are also applicable to Galileo and Beidou.

The fourth step is to modify the innovations for those measurements predicted to be NLOS. NLOS signals have a skewed error distribution as positive ranging errors are much more likely than negative. By modeling a skewed distribution within the positioning algorithm, NLOS ranging measurements may contribute to the position solution without introducing biases. However, it is more convenient to work with Gaussian distributions. Therefore, NLOS measurement innovations are adjusted to remap them onto Gaussian distributions.

The pseudorange error due to NLOS reception is always positive (Groves 2013b). By using 3D mapping, it can be shown that shorter path delays are more probable than longer delays (Hsu, 2016, private communication). However, the other contributions to the pseudorange error are conventionally modeled as zero-mean Gaussian distributions. It is therefore convenient to model the total distribution of a measurement innovation subject to NLOS reception using a skew-normal (Gaussian) distribution. By adjusting the skewness, the relative contributions of the NLOS path delay and the other pseudorange errors may be varied. The probability density function of a skew-normal distribution is given by (Azzalini 2011)

$$f_S(x) = \frac{1}{\omega\pi} \exp\left[-\frac{(x-\xi)^2}{2\omega^2}\right] \int_{-\infty}^{\alpha\left(\frac{x-\xi}{\omega}\right)} \exp\left(-\frac{t^2}{2}\right) dt \tag{4}$$

where ξ is the location, ω is the scale and α is the shape of the distribution. The mean, μ , and variance, σ^2 , are given by

$$\mu = \xi + \omega\gamma\sqrt{\frac{2}{\pi}} \quad \sigma^2 = \omega^2\left(1 - \frac{2\delta^2}{\pi}\right) \tag{5}$$

where

$$\delta = \frac{\alpha}{\sqrt{1+\alpha^2}} \tag{6}$$

To represent a GNSS measurement innovation, we can write

$$\mu = \mu_N \quad \sigma^2 = \sigma_j^2 + \sigma_r^2 + \sigma_N^2 \tag{7}$$

where σ_j is the standard deviation of all errors of the j th pseudorange measurement except for NLOS reception, σ_r is the error standard deviation of the reference satellite pseudorange measurement error (assumed LOS), σ_N is the standard deviation of the NLOS reception contribution to the pseudorange error and μ_N is the mean of the NLOS reception contribution to the pseudorange error.

Where there is no NLOS error, i.e., $\sigma_N = 0$, the shape, α , should be zero. Conversely, where there is only NLOS error, i.e., $\sigma_j = \sigma_r = 0$, the shape, α , should be infinity (giving zero probability density for negative inputs). Therefore, we can define

$$\delta = \sqrt{\frac{\sigma_N^2}{\sigma_j^2 + \sigma_r^2 + \sigma_N^2}} \quad \alpha = \sqrt{\frac{\sigma_N^2}{\sigma_j^2 + \sigma_r^2}} \tag{8}$$

Then, from (5), (7) and (8),

$$\omega^2 = \frac{(\sigma_j^2 + \sigma_r^2 + \sigma_N^2)^2}{\sigma_j^2 + \sigma_r^2 + (1 - \frac{2}{\pi})\sigma_N^2} \quad \xi = \mu_N - \sqrt{\frac{2\sigma_N^2(\sigma_j^2 + \sigma_r^2 + \sigma_N^2)}{\pi(\sigma_j^2 + \sigma_r^2) + (\pi - 2)\sigma_N^2}} \tag{9}$$

The LOS error standard deviations are computed using

$$\sigma_j = \sqrt{b_L + a_L \frac{1}{(c/n_0)_a^j}} \quad \sigma_r = \sqrt{b_L + a_L \frac{1}{(c/n_0)_a^r}} \tag{10}$$

where $(C/N_0)_a^j = 10 \log_{10}(c/n_0)_a^j$ is the measured carrier-power-to-noise density in dB-Hz. The LOS error variance coefficients, a_L , b_L , and the mean, μ_N , and standard deviation, σ_N , of the NLOS error are treated here as constants. The tuning and optimization section describes how suitable values of these parameters were determined empirically from the experimental data and provides values for each of the GNSS receivers used.

To remap an NLOS innovation (assuming the reference satellite signal is direct LOS), the cumulative distribution function (CDF) is first computed using

$$F = \frac{1}{2} \left[1 + \operatorname{erf}\left(\frac{\delta z_{pj} - \xi}{\omega\sqrt{2}}\right) \right] - 2T\left(\frac{\delta z_{pj} - \xi}{\omega}, \alpha\right) \tag{11}$$

where erf is the integral of the normal distribution, given by

$$\operatorname{erf}(x) = \frac{2}{\sqrt{\pi}} \int_0^x \exp(-t^2) dt \tag{12}$$

and T is Owen's T function, given by

$$T(x, \alpha) = \frac{1}{2\pi} \int_0^\alpha \frac{\exp(-\frac{1}{2}x^2(1+t^2))}{1+t^2} dt \tag{13}$$

where α is the shape of the distribution as defined in (8).

A standard C function is used for computing the erf function and an open source C library (<https://www.sc.fsu.edu>) is used for computing Owen’s T function.

The NLOS measurement innovation is then remapped to the corresponding direct LOS error distribution, which is a zero-mean Gaussian distribution of variance $\sigma_j^2 + \sigma_r^2$, by matching the CDF. This enables LOS and NLOS measurements to be treated the same in the position hypothesis scoring stage of the positioning algorithm.

The adjusted measurement innovation, $\delta z'_{pj}$, is thus obtained from F by solving

$$F = \frac{1}{2} \left[1 + \operatorname{erf} \left(\frac{\delta z'_{pj}}{\sqrt{2(\sigma_j^2 + \sigma_r^2)}} \right) \right] \tag{14}$$

using an open source C function for the inverse normal CDF (<https://www.sc.fsu.edu>). For each direct LOS measurement innovation, $\delta z'_{pj} = \delta z_{pj}$.

The fifth step is to score the position hypotheses. Because the measurements are differenced across satellites, all measurement innovations are correlated. Therefore, it is not possible to score individual satellites; only a joint likelihood can be computed. With the NLOS measurement innovations remapped, a multivariate zero-mean Gaussian probability distribution may be assumed. The likelihood of candidate position p is therefore

$$A_{Rp} = \begin{cases} \exp\left(-\delta \mathbf{z}_p^T \mathbf{C}_{\delta \mathbf{z}, p}^{-1} \delta \mathbf{z}'_p\right) & p \in \text{outdoor} \\ 0 & p \in \text{indoor} \end{cases} \tag{15}$$

where the modified measurement innovation vector is $\delta \mathbf{z}'_p = (\delta z'_{p1} \ \delta z'_{p2} \ \dots \ \delta z'_{pm})^T$ and the measurement error covariance matrix is

$$\mathbf{C}_{\delta \mathbf{z}} = \begin{pmatrix} \sigma_1^2 + \sigma_r^2 & \sigma_r^2 & \dots & \sigma_r^2 \\ \sigma_r^2 & \sigma_2^2 + \sigma_r^2 & \dots & \sigma_r^2 \\ \vdots & \vdots & \ddots & \vdots \\ \sigma_r^2 & \sigma_r^2 & \dots & \sigma_m^2 + \sigma_r^2 \end{pmatrix} \tag{16}$$

where m is the number of satellites tracked in addition to the reference satellite.

Probabilities can be obtained by normalizing the likelihoods, i.e., dividing by the sum of likelihoods across the search area. It is also convenient to define the log-likelihood:

$$l_{Rp} = \ln A_{Rp} = -\delta \mathbf{z}_p^T \mathbf{C}_{\delta \mathbf{z}, p}^{-1} \delta \mathbf{z}'_p \quad p \in \text{outdoor} \tag{17}$$

The final step is to determine the 3DMA likelihood-based ranging position solution. If the Easting grid coordinate of point p is E_p and the Northing coordinate is N_p , the position solution in projected coordinates is then

$$\hat{E}_R = \frac{\sum_p A_{Rp} E_p}{\sum_p A_{Rp}} \quad \hat{N}_R = \frac{\sum_p A_{Rp} N_p}{\sum_p A_{Rp}} \tag{18}$$

Similarly, the latitude and longitude are

$$\hat{L}_R = \frac{\sum_p A_{Rp} L_p}{\sum_p A_{Rp}} \quad \hat{\lambda}_R = \frac{\sum_p A_{Rp} \lambda_p}{\sum_p A_{Rp}} \tag{19}$$

It takes less than 130 ms to compute a position solution from one epoch of GNSS measurement data using a Dell Precision M2800 laptop computer with a 2.5 GHz quad-core processor and less than 290 ms using a Raspberry Pi 3. These times include the initialization algorithm.

Experimental data collection

GPS and GLONASS measurements were collected in October 2016 using a Leica Viva survey-grade GNSS receiver, illustrated in Fig. 2, a u-blox EVK M8T GNSS receiver and a HTC Nexus 9 tablet. u-blox data collection was performed by interfacing the receiver via USB to a battery-powered Raspberry Pi, which was configured as a WiFi hot spot to which a smartphone was connected (using the mobile SSH App) to configure the system and enable data logging, effectively acting as a user interface. Figure 3 illustrates the u-blox-based hardware.

The Nexus 9 tablet, shown in Fig. 4, was running the Nougat version of Android to enable capture of GNSS “raw data,” including pseudorange measurements, as well as standard NMEA messages. Data were collected using a purpose-written App. The tablet’s GNSS receiver and antenna are similar to those found on smartphones, so the results should be a good prediction of the performance of smartphones capable of logging GNSS raw data.



Fig. 2 Leica Viva GNSS receiver



Fig. 3 u-blox EVK M8T-based data logging hardware



Fig. 4 Nexus 9 tablet running Android Nougat operating system

Two rounds of data collection were performed using all three devices in two different areas of London: 5 pairs of points (10 in total), in the City of London and 4 pairs and a triplet of points (11 in total) in Canary Wharf. Figures 5 and 6 illustrate these sites. The City of London area is

typical of a traditional European city with narrow streets and buildings packed close together. The Canary Wharf area is representative of a modern city environment, found more commonly in North American and East Asian cities. The streets are wider and the buildings taller with more space between them. There is also a greater ratio of glass and steel to brick and stone than in the City of London district.

The data collection took place over 3 days. On each day, one of the three sets of GNSS equipment was used and both the City of London and Canary Wharf areas were visited. The paired locations corresponded to data collected on opposite sides of the street on the edge of the footpath next to the road. The Canary Wharf triplet of locations included a collection point located on an island in the middle of the road. The truth was established to decimeter-level accuracy using a 3D city model to identify landmarks and a tape measure to measure the relative position of the user from those identified landmarks. Before collecting data, time was allowed for the receivers to download the satellite ephemeris data and synchronize their clocks. Time synchronization requirements are the same as for conventional GNSS positioning. Interaction with the 3D mapping does not impose additional constraints. The two 4-min rounds of data at each site using each receiver were separated by approximately 2 h, ensuring that the satellite positions in the two datasets were independent. Each test location is independent of the others because 3DMA GNSS performance depends on the interaction of the satellite signals with the buildings, which are different for each location. The first dataset was used for calibration, as described in the tuning and optimization section. The second dataset

Fig. 5 Data collection sites in the City of London (Google™ earth)



Fig. 6 Data collection sites in the Canary Wharf area—London—3D view (Google™ earth)

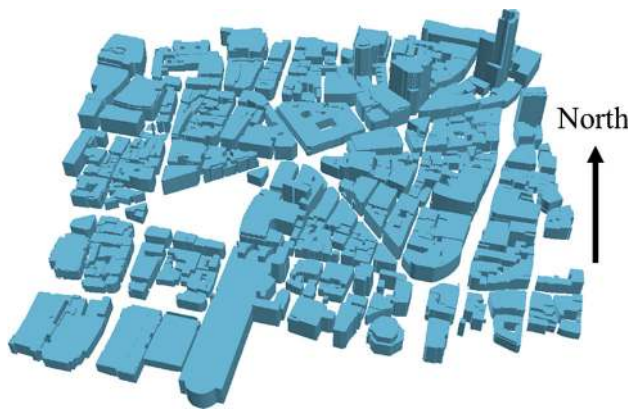


Fig. 7 3D model of City of London used in the experiments

was then used for testing the positioning algorithms as reported in the case studies and positioning performance results sections.

A 3D city model covering both areas, from Ordnance Survey (OS), was used to generate the building boundary data used for the subsequent analysis. The model is stored in the Virtual Reality Modeling Language (VRML) format. Figures 7 and 8 illustrate the 3D model used in this study.

Tuning and optimization

The likelihood-based 3DMA GNSS ranging algorithm described in the algorithm description section incorporates a number of tuning parameters. The first set of data from each site was used to determine suitable values of these parameters.

The LOS error variance coefficients, a_L and b_L , are user-equipment-dependant as both the multipath error and

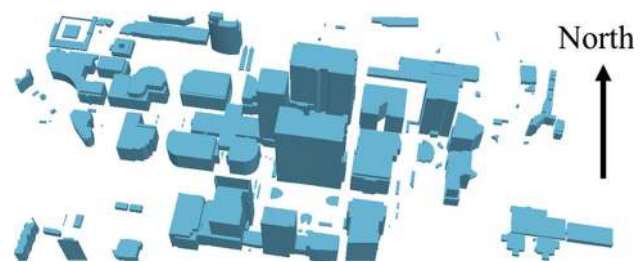


Fig. 8 3D model of Canary Wharf used in the experiments

tracking noise depend on the receiver design (Groves 2013a). Independent values were therefore determined for each of the three receivers using the measurements from all test sites that were predicted to be direct LOS using the building boundary and the true position. Pseudorange errors were estimated by differencing measured pseudoranges with corresponding pseudoranges computed using the true position and the receiver clock offset solution. The clock offset was obtained by conventional GNSS least squares positioning using only those satellites predicted to be direct LOS at the true position.

A pseudorange error variance was then computed for each value of C/N_0 . The values of a_L and b_L used in the likelihood-based 3DMA GNSS ranging algorithm were then determined by fitting a linear function, $Y = b_L + a_L X$ to the data. Figure 9 illustrates the relationship between the LOS pseudorange error standard deviation and C/N_0 for the u-blox receiver.

The mean, μ_N , and standard deviation, σ_N , of the NLOS error are treated as receiver-independent constants. In practice, they will be environment dependent. However, the aim here was to find a single pair of values that are suitable for all of the test sites. The values of both μ_N and σ_N were, therefore, varied from 20 to 60 m with a step of

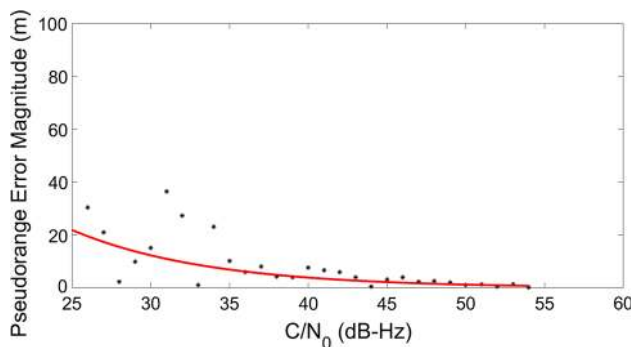


Fig. 9 u-blox receiver LOS pseudorange standard deviation as a function of C/N_0 . The black stars show the measured values and the red line shows the function fitted to these values

Table 1 Likelihood-based 3DMA GNSS ranging algorithm tuning parameters

Parameter	Leica Viva	u-blox EVK M8T	Nexus 9 tablet
LOS error variance coefficient a_L (m^2 Hz)	19,500	205,700	297,500
LOS error variance coefficient b_L (m^2)	3	18.72	87.72
NLOS error mean, μ_N (m)	50	50	50
NLOS error standard deviation, σ_N (m)	35	35	35

5 m and values selected that minimized the root-mean-square (RMS) position error across all test sites.

Table 1 lists the values of the tuning parameters used for the tests presented in the following sections.

Case studies

Likelihood-based 3DMA GNSS ranging (LBR) scoring maps for test site 3, City of London, are presented in Figs. 10, 11 and 12 for the Leica Viva, u-blox and Nexus 9 data, respectively. In each figure, the black star represents the true position, the white star the LBR solution, the blue star the least squares 3DMA GNSS ranging (LSR) solution and the red star the conventional GNSS solution. In all cases, the LBR position solution is much closer to the true position than either the LSR or conventional position solution. The highest scoring candidate positions are all clustered within a few meters with the other candidate positions scoring much lower. However, significant differences between the three receivers can be observed. The incorrect candidate positions score significantly lower using the Viva data and significantly higher using the Nexus 9 data, with the scores from the u-blox receiver in-between the other two. Thus, the receiver and antenna

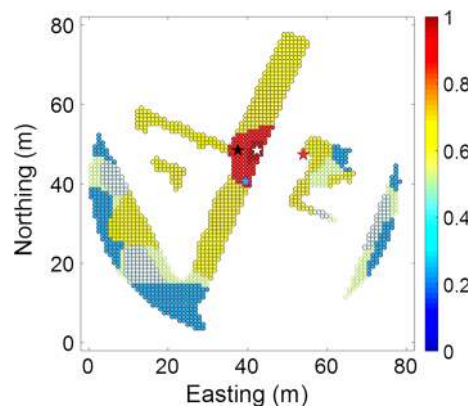


Fig. 10 Likelihood-based 3DMA GNSS scoring map—Leica Viva receiver, City of London, location 3

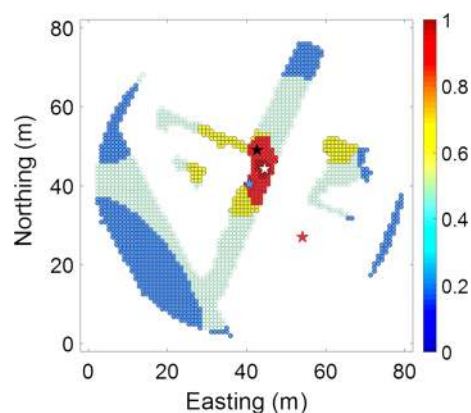


Fig. 11 Likelihood-based 3DMA GNSS scoring map—u-blox receiver, City of London, location 3

quality does have a notable effect. Figure 13 illustrates further examples of the LBR scoring maps from the u-blox data in the City of London and Canary Wharf area. In each case, the LBR solution is closest to the true position and the conventional GNSS solution furthest away.

Positioning performance results

Table 2 shows the root-mean-square (RMS) single-epoch position errors obtained with the three receivers using the new likelihood-based 3DMA GNSS ranging algorithm, the least squares 3DMA GNSS ranging algorithm described in Adjrad and Groves (2017) and a conventional GNSS positioning algorithm. Along-street, across-street and horizontal (i.e., 2 dimensional) RMS position errors are shown for each site. Figure 14 shows the all-site horizontal RMS position errors for each receiver and positioning method.

Examining the results shows that the new likelihood-based 3DMA GNSS ranging method consistently outperforms both of the other methods. It is nearly twice as accurate as the least

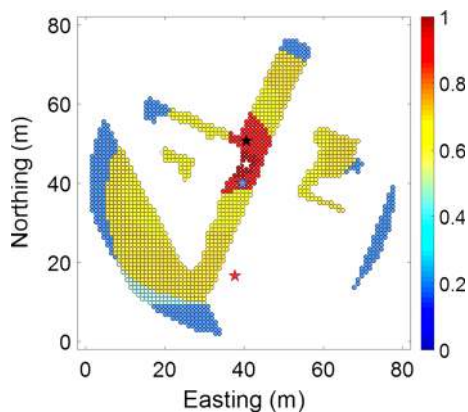


Fig. 12 Likelihood-based 3DMA GNSS scoring map—Nexus 9 receiver, City of London, location 3

squares 3DMA ranging algorithm and four to five times as accurate as conventional GNSS positioning. Both the Leica and u-blox receivers give more accurate results than the Nexus 9 tablet. This is because the tablet has a linearly polarized GNSS antenna, like on a smartphone. Linearly polarized antennas do not distinguish between the right-hand circular polarization (RHCP) of the signals received directly from the satellite and the left-hand circular polarization (LHCP) or mixed polarization of the reflected signals. By contrast, the

u-blox and Leica receivers use circularly polarized antennas that attenuate LHCP signals compared to RHCP signals. Consequently, the pseudorange measurements made by the tablet exhibit larger multipath errors, resulting in larger position errors with all three positioning methods.

Using all three positioning methods, the Leica receiver is slightly more accurate than the u-blox receiver overall, though the u-blox receiver performed better at many of the City sites. This is because the survey-grade Leica equipment has an antenna with high polarization discrimination and its receiver has a high bandwidth, enabling more sophisticated correlator-based multipath mitigation. Leica pseudorange measurements are also carrier-smoothed. However, most practical applications of 3DMA GNSS would use a smartphone or a consumer-grade receiver.

Comparing the two test areas shows that the Canary Wharf sites were more challenging than the City of London sites with larger RMS position errors for all receivers and methods. This could be because the buildings are generally further apart so the path delays of the NLOS signals are higher. The reflected signals are also stronger because metallized glass is a stronger reflector at GNSS wavelengths than brick and stone. Comparing the along-street and across-street results, it can be seen that the across-street errors are larger for all receivers and positioning

Fig. 13 Likelihood-based 3DMA GNSS scoring map—u-blox receiver, City of London (top two plots Locations 2 and 5) and Canary Wharf (bottom two plots Locations 1 and 3)

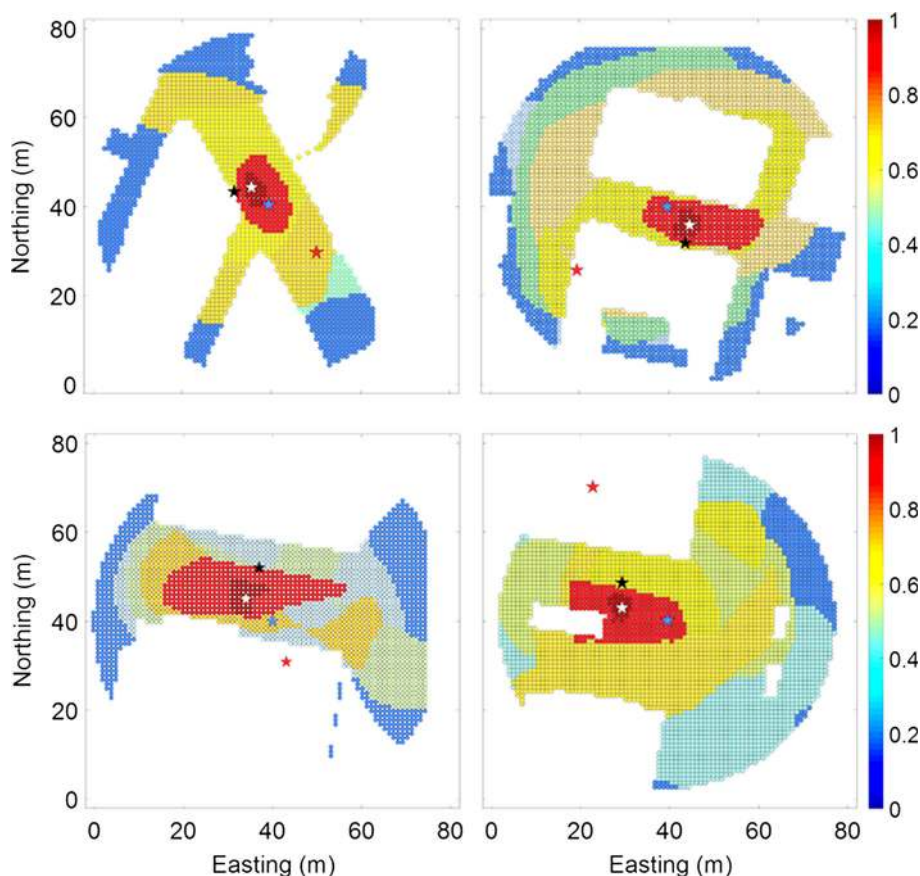


Table 2 RMS position errors for different positioning methods, receivers and test sites

Receiver	Method	Along-street RMS error (m)		Across-street RMS error (m)		Horizontal RMS error (m)	
		City	Canary Wharf	City	Canary Wharf	City	Canary Wharf
Leica Viva	Conventional	4.4	4.7	18.0	21.9	18.5	22.4
	Least squares 3DMA ranging	3.3	2.7	5.7	7.2	6.6	7.7
	Likelihood-based 3DMA ranging	1.8	2.3	3.9	4.5	4.3	5.1
u-blox EVK M8T	Conventional	7.2	11.0	12.8	28.6	14.7	30.7
	Least squares 3DMA ranging	3.1	5.5	4.2	9.7	5.3	11.1
	Likelihood-based 3DMA ranging	2	3.9	3.3	6.2	3.9	7.3
Nexus 9 tablet	Conventional	10.3	19.6	19.9	27.9	22.4	34.1
	Least squares 3DMA ranging	4.0	6.5	6.6	10.0	7.7	11.9
	Likelihood-based 3DMA ranging	3	4	3.4	7.4	4.5	8.4

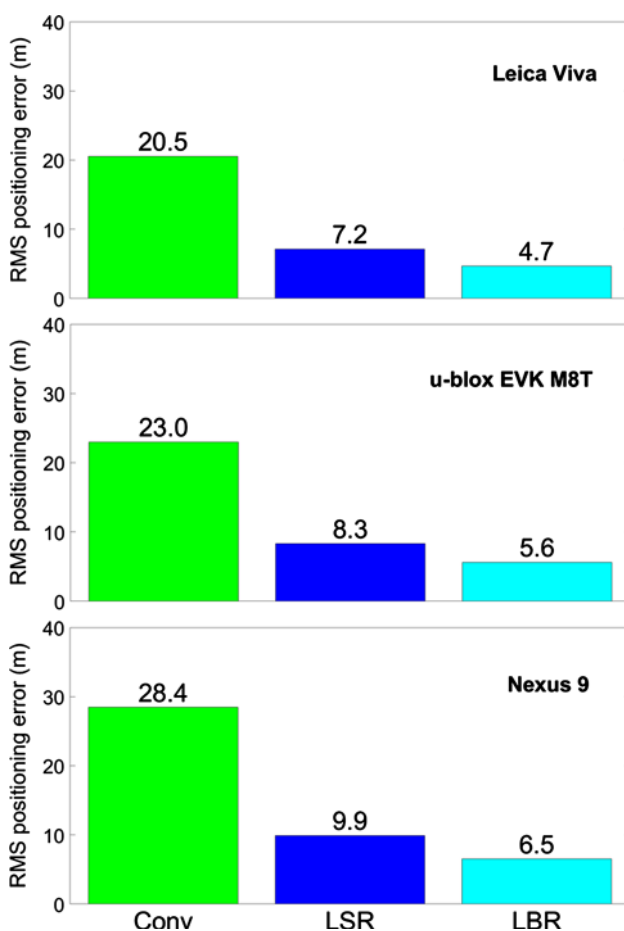


Fig. 14 Overall horizontal RMS positioning errors using each receiver. The *green bars* show the conventional GNSS positioning (Conv) errors, the *dark blue bars* show the LSR positioning errors and the *light blue bars* show the LBR positioning errors

methods. This is because more GNSS signals are blocked in the across-street direction, resulting in better signal geometry (and thus lower dilution of precision) in the along-street direction.

Conclusions, future and related work

A likelihood-based 3D-mapping-aided GNSS ranging algorithm has been demonstrated that enables those signals predicted to be non-line-of-sight to contribute to the position solution without explicitly computing the additional path delay due to NLOS reception. Likelihoods for an array of candidate positions are computed based on the difference between the measured and predicted pseudoranges. However, a skewed distribution is assumed for those signals predicted to be NLOS on the basis that the ensuing ranging errors are always positive. Horizontal RMS single-epoch position accuracies of 4.7, 5.6 and 6.5 m are obtained in dense urban areas using data from, respectively, a Leica Viva geodetic receiver, a u-blox EVK M8T consumer-grade receiver and a Nexus 9 tablet incorporating smartphone GNSS antenna and chipset that outputs pseudoranges. These results constitute a factor of four accuracy improvement over single-epoch conventional GNSS positioning using the same measurements. They are also 35% more accurate than results obtained using a 3D-mapping-aided least squares GNSS positioning algorithm. The difference in performance between the different receivers reflects their differing susceptibility to multipath interference due to variations in antenna quality and receiver bandwidth.

There are many potential topics for further research. The models of the pseudorange error distributions of both the NLOS and the direct-LOS signals could be improved. Examination of the pseudorange error statistics of the direct LOS signals suggests a potential dependence on the elevation angle in addition to the C/N_0 dependence. Thus, including an elevation-dependent term in the LOS error standard deviation used within the likelihood-based 3DMA ranging algorithm has the potential to improve performance. Further experimental data are needed to quantify this and determine a suitable model. Elevation-dependent

modeling of the NLOS error distribution should also be investigated. Simple parameters derived from the 3D mapping, such as street width, could also potentially contribute.

Here, only single-epoch positioning is considered. However, conventional GNSS receivers improve accuracy and reliability by also computing a velocity solution and using this to filter the position solution over multiple epochs, smoothing many of the error sources. Similar benefits can be expected from filtering 3DMA GNSS positioning. Therefore, a multi-epoch version of the likelihood-based 3DMA ranging algorithms presented here is a high priority.

The results presented here use only GPS and GLONASS signals. Adding Galileo and Beidou signals should improve performance, particularly once those constellations reach full maturity. 3DMA GNSS positioning could also be deployed on micro air vehicles operating in urban areas. A 3D position search area would be computationally expensive. However, use of a height solution from a barometric, radar or ultrasonic altimeter enables the search area to be constrained to two dimensions as for terrestrial applications. There's also the potential to deploy 3DMA GNSS ranging indoors, possibly in combination with high-sensitivity signal processing techniques.

As shown in Table 2, 3DMA GNSS ranging produces a position solution which is more accurate in the along-street direction than the across-street direction. GNSS shadow matching works better in the across-street direction. The two techniques are therefore complementary and, as they share the same building boundary data, derived from 3D mapping, they are also synergistic. It is thus logical to integrate the two techniques. Preliminary results presented in Adjrad and Groves (2016) show that integrated 3DMA GNSS positioning is consistently more accurate than either shadow matching or 3DMA ranging on their own. Optimization of the integration algorithms and further data collection is currently ongoing.

Regarding practicality, UCL's 3DMA GNSS algorithms have been implemented in real time on a Raspberry Pi 3 at a 1-Hz update rate. Thus, implementation on a smartphone with a GNSS chip that outputs pseudorange measurements is also feasible. Sourcing and distribution of the 3D mapping or building boundary data is discussed in Groves (2016), while assisted GNSS could be used to provide satellite ephemeris data and receiver clock synchronization. A further practical consideration is determining when to use 3DMA GNSS, when to use conventional GNSS positioning and when to use alternative positioning technologies. To address this, context determination algorithms for distinguishing open, urban and indoor environments using GNSS data are under development (Gao and Groves 2016).

Acknowledgement This work is funded by the Engineering and Physical Sciences Research Council (EPSRC) Project EP/L018446/1, *Intelligent Positioning in Cities using GNSS and Enhanced 3D Mapping*. The project is also supported by Ordnance Survey, u-blox and the Royal National Institute for Blind People. The authors would also like to thank Canary Wharf Group plc, particularly Ms Lesley Johnson – Canary Wharf Central Records Manager, for their permission to collect GNSS data in the Canary Wharf Estate.

Open Access This article is distributed under the terms of the Creative Commons Attribution 4.0 International License (<http://creativecommons.org/licenses/by/4.0/>), which permits unrestricted use, distribution, and reproduction in any medium, provided you give appropriate credit to the original author(s) and the source, provide a link to the Creative Commons license, and indicate if changes were made.

References

- Adjrad M, Groves PD (2016) Intelligent urban positioning using shadow matching and GNSS ranging aided by 3D mapping. In: Proceedings of the ION GNSS+ 2016. Institute of Navigation, Portland, OR, September, pp 534–553
- Adjrad M, Groves PD (2017) Enhancing least squares GNSS positioning with 3D mapping without accurate prior knowledge. Accepted for publication in navigation (preliminary version published at ION GNSS+ 2015)
- Amt JR, Raquet JF (2006) Positioning for range-based land navigation systems using surface topography. In: Proceedings of ION GNSS 2006. Institute of Navigation, Fort Worth, TX, September, pp 1494–1505
- Anon (2008) Global navigation satellite system GLONASS interface control document, Edition 5.1. Russian Institute of Space Device Engineering
- Azzalini A (2011) Skew normal distribution. In: Lovric M (ed) International encyclopedia of statistical science, vol 19. Springer, Heidelberg, pp 1342–1344
- Ben-Moshe B et al (2011) Improving accuracy of GNSS devices in urban canyons. In: Proceedings of 23rd Canadian conference on computational geometry
- Betaille D et al (2013) A new modeling based on urban trenches to improve GNSS positioning quality of service in cities. IEEE Intell Transp Syst Mag 5(3):59–70
- Bhuiyan MZH, Lohan ES (2012) Multipath mitigation techniques for satellite-based positioning applications. In: Jin S (ed) Global navigation satellite systems: signal, theory and applications. InTech, Winchester, pp 405–426
- Bourdeau A, Sahmoudi M (2012) Tight integration of GNSS and a 3D city model for robust positioning in urban canyons. In: Proceedings of ION GNSS 2012. Institute of Navigation, Nashville, TN, September, pp 1263–1269
- Bradbury J, Ziebart M, Cross PA, Boulton P, Read A (2007) Code multipath modelling in the urban environment using large virtual reality city models: determining the local environment. J Navig 60(1):95–105
- Gao H, Groves PD (2016) Context determination for adaptive navigation using multiple sensors on a smartphone. In: Proceedings of ION GNSS+ 2016. Institute of Navigation, Portland, OR, September, pp 742–756
- Groves PD (2011) Shadow matching: a new GNSS positioning technique for urban canyons. J Navig 64(3):417–430
- Groves PD (2013a) Principles of GNSS, inertial, and multi-sensor integrated navigation systems, 2nd edn. Artech House, Boston

- Groves PD (2013b) GNSS solutions: multipath vs. NLOS signals. How does non-line-of-sight reception differ from multipath interference. *Inside GNSS* 8(6):40–42, 63
- Groves PD (2016) It's time for 3D-Mapping-Aided GNSS. *Inside GNSS* 11(5):50–56
- Groves PD, Wang L, Adjrad M, Ellul C (2015) GNSS shadow matching: the challenges ahead. In: *Proceedings of ION GNSS+ 2015*. Institute of Navigation, Tampa, FL, pp 2421–2443
- Gu Y, Hsu L-T, Wada Y, Kamijo S (2015) Integration of 3D map based GPS positioning and on-board sensors for vehicle self-localization in urban canyon. In: *Proceedings of ION 2015 Pacific PNT meeting*, Honolulu, Hawaii, pp 565–572
- Hsu L-T, Gu Y, Kamijo S (2015) 3D building model-based pedestrian positioning method using GPS/GLOANSS/QZSS and its reliability calculation. *GPS Solut*. doi:10.1007/s10291-015-0451-7
- Kumar R, Petovello MG (2014) A novel GNSS positioning technique for improved accuracy in urban canyon scenarios using 3D city model. In: *Proceedings of ION GNSS+ 2014*. Institute of Navigation, Tampa, FL, September, pp 2139–2148
- Neil AE (1996) Global mapping for the atmospheric delay at radio wavelengths. *J Geophys Res* 111(B2):3227–3246
- Obst M, Bauer S, Wanielik G (2012) Urban multipath detection and mitigation with dynamic 3D maps for reliable land vehicle localization. In: *Proceedings of IEEE/ION position, location and navigation symposium (PLANS)*, Myrtle Beach, SC, April, pp 685–691
- Peyraud S et al (2013) About non-line-of-sight satellite detection and exclusion in a 3D map-aided localization algorithm. *Sensors* 13:829–847
- Suh Y, Shibasaki R (2007) Evaluation of satellite-based navigation services in complex urban environments using a three-dimensional GIS. *IEICE Trans Commun E90-B*:1816–1825
- Suzuki T (2016) Integration of GNSS positioning and 3D map using particle filter. In: *Proceedings of ION GNSS+ 2016*. Institute of Navigation, Portland, OR, September, pp 1296–1304
- Suzuki T, Kubo N (2012) GNSS positioning with multipath simulation using 3D surface model in urban canyon. In: *Proceedings of ION GNSS 2012*. Institute of Navigation, Nashville, TN, September, pp 438–447
- Suzuki T, Kubo N (2013) Correcting GNSS multipath errors using a 3D surface model and particle filter. In: *Proceedings of ION GNSS+ 2013*. Institute of Navigation, Nashville, TN, September, pp 1583–1595
- Wang L, Groves PD, Ziebart MK (2012) Multi-constellation GNSS performance evaluation for urban canyons using large virtual reality city models. *J Navig* 65(3):459–476
- Wang L, Groves PD, Ziebart MK (2013) GNSS shadow matching: improving urban positioning accuracy using a 3D city model with optimized visibility prediction scoring. *Navigation* 60(3):195–207
- Wang L, Groves PD, Ziebart MK (2015) Smartphone shadow matching for better cross-street GNSS positioning in urban environments. *J Navig* 68(3):411–433
- Yozevitch R, Ben-Moshe B (2015) A robust shadow matching algorithm for GNSS positioning. *Navigation* 62(2):95–109



Navigation and a recipient of the ION Thurlow Award.



Dr. Paul D. Groves is a Senior Lecturer (associate professor) at University College London (UCL). He is interested in all aspects of navigation and positioning, including improving GNSS performance under challenging reception conditions, advanced multisensor integrated navigation and novel positioning techniques. He is author of the book *Principles of GNSS, Inertial and Multi-Sensor Integrated Navigation Systems*, a fellow of the Royal Institute of

Dr. Mounir Adjrad is a Post-doctoral Research Associate at UCL. His current research interests focus on Intelligent Urban Positioning, exploiting conventional GNSS technology augmented by 3D models of urban environments. He has research experience in industry and academic institutions working on topics such as ultra-wideband technology, GNSS, satellite engineering, radar, biomedical engineering and transport engineering.